Wiley Online Library
Early View publication on www.wileyonlinelibrary.com
(issue and page numbers not yet assigned;
citable using Digital Object Identifier – DOI)

J. Biophotonics 1–15 (2016) / **DOI** 10.1002/jbio.201600193

Journal of BIOPHOTONICS

FULL ARTICLE

Remission spectrometry for blood vessel detection during stereotactic biopsy of brain tumors

*Niklas A. Markwardt**, **, [1, 2], *Herbert Stepp*[1, 2], *Gerhard Franz*[3], *Ronald Sroka*[1, 2], *Marcus Goetz*[4], *Petr Zelenkov*[5], *and Adrian Rühm*[1, 2]

[1] Laser-Forschungslabor, LIFE Center, University Hospital of Munich, Munich, Germany
[2] Department of Urology, University Hospital of Munich, Munich, Germany
[3] Department of Applied Sciences and Mechatronics, Munich University of Applied Sciences, Munich, Germany
[4] MRC Systems GmbH, Heidelberg, Germany
[5] Burdenko Neurosurgery Institute, Moscow, Russia

Received 5 July 2016, revised 14 September 2016, accepted 15 September 2016
Published online 10 October 2016

Key words: stereotactic biopsy, glioblastoma multiforme, hemorrhage, blood vessel detection, optical phantoms, ray tracing simulations

Stereotactic biopsy is used to enable diagnostic confirmation of brain tumors and treatment planning. Despite being a well-established technique, it is related to significant morbidity and mortality rates mostly caused by hemorrhages due to blood vessel ruptures.

This paper presents a method of vessel detection during stereotactic biopsy that can be easily implemented by integrating two side-view fibers into a conventional side-cutting biopsy needle. Tissue within the needle window is illuminated through the first fiber; the second fiber detects the remitted light. By taking the ratio of the intensities at two wavelengths with strongly differing hemoglobin absorption, blood vessels can be recognized immediately before biopsy sampling.

Via ray tracing simulations and phantom experiments, the dependency of the remission ratio $R = I_{578}/I_{650}$ on various parameters (blood oxygenation, fiber-to-vessel and inter-fiber distance, vessel diameter and orientation) was investigated for a bare-fiber probe. Up to 800–1200 µm away from the probe, a vessel can be recognized by a considerable reduction of the remission ratio from the background level. The technique was also successfully tested with a real biopsy needle probe on both optical phantoms and *ex-vivo* porcine brain tissue, thus showing potential to improve the safety of stereotactic biopsy.

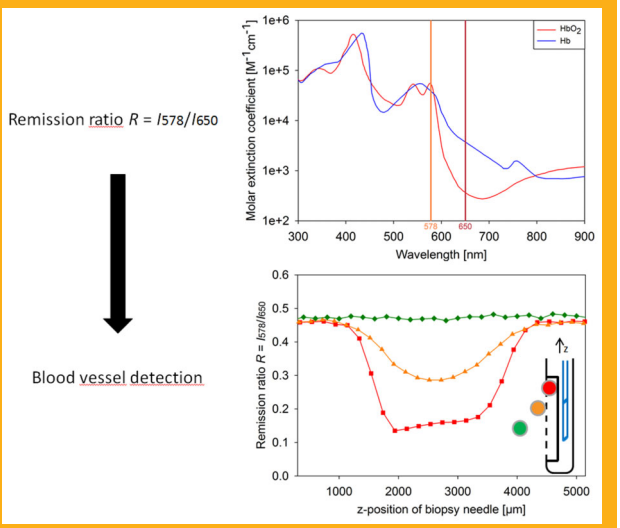

Dual-wavelength remission measurement for the detection of blood vessels during stereotactic biopsy.

* Corresponding author: e-mail: Niklas.Markwardt@med.uni-muenchen.de, Phone: +49 89 4400 74880, Fax: +49 89 4400 74864
** This manuscript is part of the inaugural thesis of Niklas Markwardt to be submitted at the Medical Faculty of the Ludwig-Maximilians-Universität, Munich.

Journal of BIOPHOTONICS

1. Introduction

Stereotactic biopsy is a well-established method in neurosurgery. It is applied for the diagnosis of cerebral neoplasms if radiographic information is insufficient or for diagnostic confirmation and treatment planning in case open resection is not possible [1].

Among the group of gliomas, which account for about 80% of all primary malignant brain tumors, glioblastoma multiforme represents the most prevalent and malignant tumor type [2, 3]. With a 5-year survival rate of less than ~5% [3, 4], its prognosis is very poor. Chemotherapy based on alkylating agents such as temozolomide is a promising therapeutic option for patients with a methylated O^6-methylguanine-DNA methyltransferase (MGMT) gene promoter [5]. Stereotactic biopsy may be used to assess this MGMT status as well as further biomarkers that influence prognosis and enable personalized treatment such as the proliferative index Ki-67, mutations on the isocitrate dehydrogenase genes IDH1/2, and alterations of chromosome arms 1p and 19q [6–8].

The principle of stereotactic biopsy is illustrated in Figure 1a. To obtain a tissue sample, a biopsy needle is attached to the stereotactic frame and inserted into the brain along a predefined trajectory until the distal needle end is positioned in an area of vital tumor. Despite its broad application, stereotactic biopsy is associated with significant risks. Mortality [1, 11–13] and serious morbidity [12–15] rates of up to 3.8% and 12%, respectively, have been reported. Most complications are caused by hemorrhages, which can lead to severe neurological deficits or death. Malone et al. report on a biopsy-related mortality of 13% in case a hemorrhage was observed during biopsy, which was six-fold higher than for all other patients [1]. In most studies, moderate occurrence rates of hemorrhages ranging from 0.3% to 7% are indicated [1, 15–17], but Kulkarni et al. [11] found an alarmingly high rate of silent hemorrhages (54%), which occasionally lead to delayed neurological deficits. Given these numbers, a stereotactic device would be desirable that is capable of detecting larger blood vessels during intervention to avoid rupture by the biopsy needle.

There have already been several approaches to detect blood vessels during stereotactic biopsy or similar neurosurgical interventions, including Doppler sonography [18], laser Doppler flowmetry (LDF) [19], Indocyanine Green (ICG) fluorescence [20], and interstitial optical tomography (iOT) [21, 22]. Especially LDF, which seems to be the method with the highest clinical potential, has already been tested in surgical interventions [23, 24]. So far, however, none of these attempts has been routinely implemented in stereotactic biopsy, for some of these methods probably due to the required sophisticated probe.

In this paper, a comparatively simple technique is presented that may be permanently integrated into a side-cutting biopsy needle (cf. Figure 2c). It is conceived for blood vessel detection within the tissue volume contained inside the suction window where the risk of vessel rupture is maximal, namely during the step of tissue sampling. Due to the rounded distal end of the biopsy needle, blood vessels in front of the needle that might get hit during needle insertion are at considerably lower risk as they would most probably be pushed aside and not be ruptured. The method is based on the characteristic spectral dependence of the absorption of hemoglobin (Figure 1b). The probed tissue is illuminated (e.g. with a broadband light source) and the remitted light intensity is recorded at two wavelengths with highly differing hemoglobin absorption (e.g. 578 nm and 650 nm). 578 nm was selected as first wavelength be-

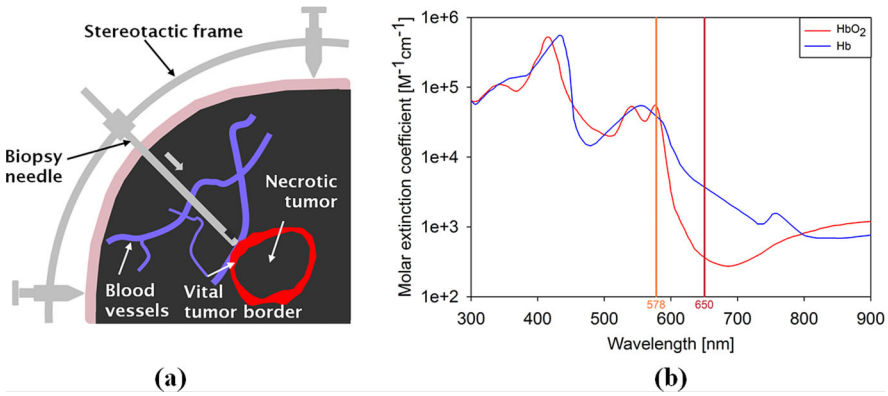

Figure 1 (**a**) Stereotactic biopsy of brain tumors. A biopsy needle is attached to the stereotactic frame and inserted into the brain along a predefined trajectory (indicated by the arrow) until the distal needle end is positioned in an area of vital tumor tissue. (Adapted with permission from Markwardt et al. [9].) (**b**) Molar extinction coefficients of oxygenated (HbO_2) and deoxygenated (Hb) hemoglobin. The wavelengths 578 nm and 650 nm are indicated by orange and dark red lines, respectively. (Data taken from Prahl [10].)

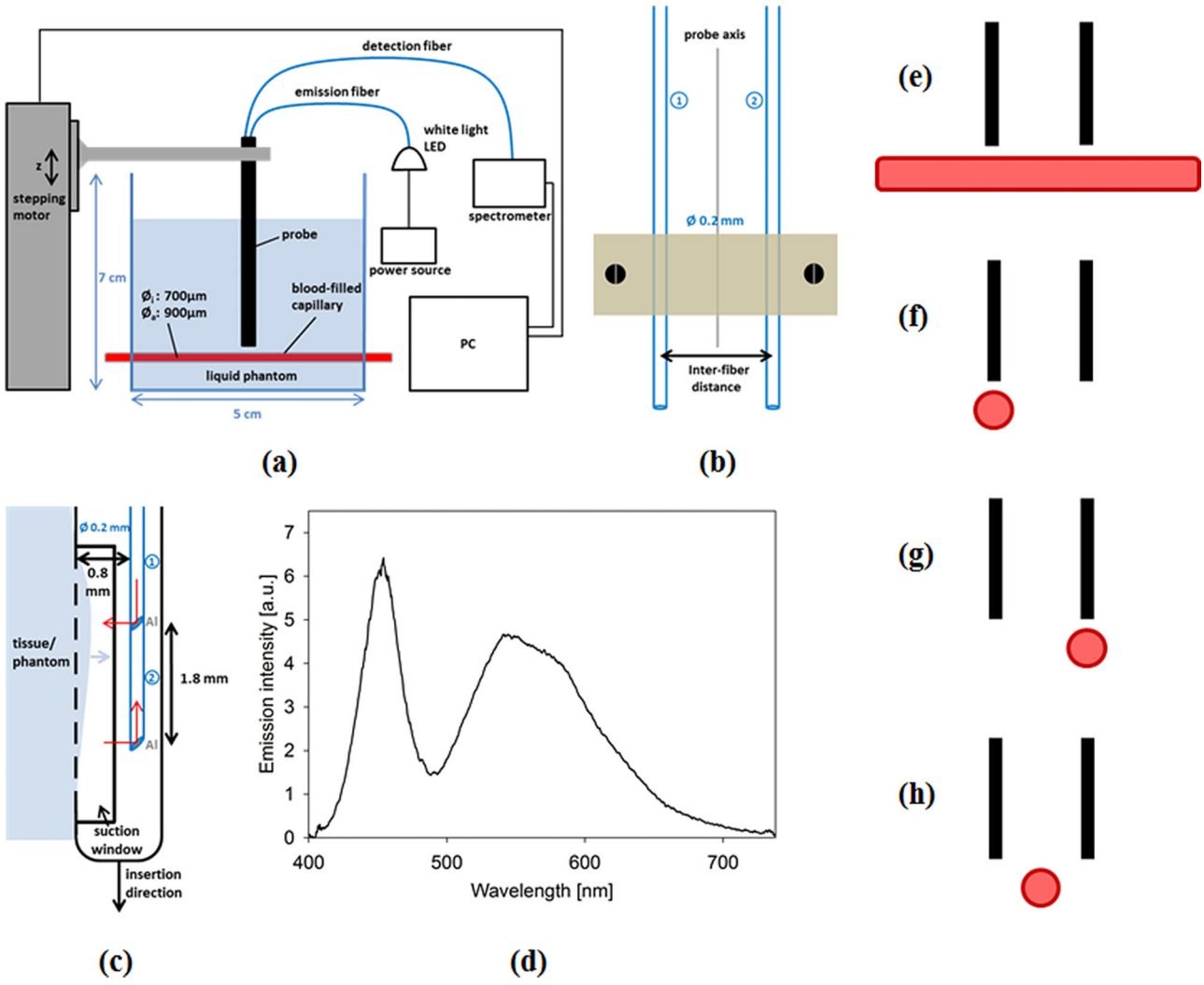

Figure 2 (**a**) Sketch of the setup used for phantom experiments. The liquid phantom was filled into a cylindrical container (drawn in blue), which incorporated a blood-filled glass capillary simulating a blood vessel. For the tissue experiments, the phantom container was replaced with a beaker containing the investigated tissue. The probe could be moved with a computer-controlled stepping motor. Light of a broadband LED was coupled into the emission fiber; the remission light was collected with the detection fiber and guided to a spectrometer. (**b**) Bare-fiber probe consisting of polished crosscut fibers (core diameter: 0.2 mm) fixed between two screwable plastic blocks (1: emission fiber, 2: detection fiber). (**c**) Needle probe consisting of a biopsy needle with integrated aluminum-coated (Al) side-view fibers (1: emission fiber, 2: detection fiber, core diameter: 0.2 mm). (**d**) LED emission spectrum acquired with the bare-fiber probe via reflection from a white remission standard, normalized to 1 at 650 nm. Blood vessel orientations used for experiments and simulations: (**e**) coplanar, (**f**) perpendicular, ahead of emission fiber, (**g**) perpendicular, ahead of detection fiber, (**h**) perpendicular, between fibers.

cause it is associated with a local absorption maximum of oxygenated hemoglobin (the global maximum slightly above 400 nm would have provided even higher hemoglobin absorption, but also a tissue penetration depth that would have been too low for a reasonable blood vessel detection range resulting from the combination of both wavelengths). The choice of 650 nm as second wavelength was the result of a trade-off between the highest possible difference in hemoglobin absorption and technical practicability (evaluation around 700 nm would have provided even lower hemoglobin absorption, but also very low remission intensity values due to the emission characteristics of typical white light LEDs, cf. e.g. Figure 2d). Phantom and tissue experiments as well as ray tracing simulations were used to demonstrate the functionality of this technique.

2. Materials and methods

2.1 Experimental setup

2.1.1 Overview

The experiments conducted on optical phantoms are described in detail in Section 2.2.1, the experiments on biological tissue (taken from the slaughterhouse) in Section 2.2.2. The setup for the phantom experiments is shown in Figure 2a. A liquid phantom, mimicking tissue optical properties, was poured into a plastic container whose inner walls were coated with black paint to avoid reflections. To simulate a blood vessel, a cylindrical glass capillary (inner diameter: 700 µm, wall thickness: 100 µm) was filled with fresh heparinized blood, sealed with modeling clay, and inserted into the container through two diametrically opposed holes. In the following, the term *fiber-to-capillary distance* always refers to the distance of the fiber tips from the inner surface of the capillary wall.

Remission measurements were performed with a two-fiber probe (Section 2.1.2). Light from a broadband light emitting diode (LED) (APG2C3-NW, Roithner Lasertechnik GmbH, Vienna, Austria) with a total output power of 500 mW, measured with a powermeter (thermal head LM-10, Coherent, Inc., Santa Clara, CA, USA), was coupled into the emission fiber. The light power that was coupled out of the distal end of the emission fiber was 70 µW, yielding a maximum irradiance (directly at the distal fiber end) of about 2.2 kW/m^2, which approximately corresponds to the maximum permissible exposure (MPE) for the skin in the employed wavelength range (2 kW/m^2) [25]. A normalized emission spectrum of the LED is shown in Figure 2d; it was acquired with the bare-fiber probe via reflection from a white reflectance standard with a reflectivity of $99 \pm 0.5\%$ in the employed wavelength range (SG 3054/26, LOT-Oriel GmbH, Darmstadt, Germany) and the same spectrometer as in the following experiments. The remitted light was collected with the detection fiber and guided to a spectrometer (AVS-USB2000, Avantes, Inc., Broomfield, CO, USA), which – in combination with the 200 µm detection fiber (see Section 2.1.2) – provided a spectral resolution of 5 nm at both exploited wavelengths (578 nm and 650 nm) and which was readout via OOIBase32 (Ocean Optics GmbH, Ostfildern, Germany). The integration time was set to 75 ms, 300 ms and 900 ms for investigating inter-fiber distances of 1 mm, 2 mm and 3 mm, respectively. The use of a spectrometer instead of, for instance, two detection channels with narrowband filters and less expensive photodiodes provided the possibility to obtain additional evidence for the presence of blood in front of the fiber probe beyond the ratio of the remitted intensities at 578 nm and 650 nm, i.e. the identification of the characteristic absorption maxima of oxygenated hemoglobin at around 540 nm and 580 nm in the remission spectra. A LabVIEW-controlled stepping motor with 2.5 µm precision enabled accurate probe displacements in z-direction. For the tissue experiments, the same setup was employed; only the phantom container with embedded glass capillary was replaced with a beaker containing porcine brain tissue with naturally incorporated blood vessels.

2.1.2 Optical probes

Two different optical probes were used to deliver light to or from the phantom or tissue sample: a *bare-fiber probe* consisting of two crosscut optical fibers (Figure 2b) and a *needle probe* consisting of a biopsy needle with two integrated side-view fibers (Figure 2c). In a first step (Section 3.1.1), the bare-fiber probe was used for experimental simplicity and accuracy to investigate in phantom experiments the dependencies of the remission signal on different parameters like inter-fiber distance, fiber-to-vessel distance and relative vessel orientation. In a second step, the functionality of the needle probe, as it is intended to be applied clinically, was checked in phantom (Section 3.2.1) and tissue (Section 3.2.2) experiments. Both probes were based on polyimide-coated silica fibers (UM22-200, Thorlabs GmbH, Dachau, Germany) with a core diameter of 200 µm, an outer diameter of 240 µm, and a numerical aperture (NA) of 0.22.

For the bare-fiber probe, two polished crosscut fibers were fixed, parallel to each other, to a special fiber holder consisting of two screwable plastic blocks. Grooves of 0.5 mm thickness and 1 mm separation (center-to-center) were milled into one of the blocks to guarantee a well-defined inter-fiber distance, which was varied between 1 mm and 3 mm (axis-to-axis). After fastening the fibers to the holder, the actual distance between the distal fiber ends was controlled with a high-precision ruler (uncertainty: ±0.2 mm); their separation from the fiber holder along the fiber axis was several centimeters to exclude signal falsification by light reflections.

The needle probe was constructed by gluing two side-view fibers into the inner cannula (inner/outer diameter: 1.1/1.4 mm, respectively) of a PAJUNK® BrainPro biopsy cannula set (Pajunk GmbH, Geisingen, Germany). This inner cannula can be turned relative to an outer cannula (1.4/1.8 mm, not shown in Figure 2c) to shear off tissue extending into the suction window. Side-view fibers were produced by grinding the distal fiber ends at an inclination angle of 45° and subsequently coating the ground surfaces with aluminum in a high-vacuum vapor coating sys-

Table 1 Optical properties of the liquid phantom: aspired literature data for brain tumor tissue [26–28] and experimentally achieved data measured with an integrating sphere (mean values ± one standard deviation).

Wavelength [nm]	μ_a [mm^{-1}]		μ_s' [mm^{-1}]	
	aspired	achieved	aspired	achieved
578	0.21 ± 0.09	0.22 ± 0.02	1.8 ± 1.0	1.9 ± 0.2
650	0.068 ± 0.038	0.074 ± 0.007	1.6 ± 0.9	1.7 ± 0.2

tem. The distal ends of the fibers were placed within the suction window adjacent to each other, with a positional offset of (1.8 ± 0.2) mm parallel to the fiber axes. The viewing directions of the side-view fibers were aligned into the direction of the needle opening with an estimated accuracy of ±10°.

2.1.3 Liquid phantom

The liquid phantom was designed to mimic brain tumor optical properties at the wavelengths 578 nm and 650 nm. Lipovenös® (Fresenius Kabi GmbH, Bad Homburg, Germany) as well as a mixture of ink ("brilliant black 4001") and India ink ("Tusche A", black, both from Pelikan GmbH, Hannover, Germany) were used to reproduce reduced scattering ($\mu_s' = \mu_s \cdot (1 - g)$, where μ_s and g denote scattering coefficient and anisotropy) and absorption (μ_a) coefficients, respectively. For this purpose, data published by Gebhart et al. (glioma, determined *in vitro* on n = 39 samples) [26], Yaroslavsky et al. (astrocytoma, *in vitro*, n = 4) [27] and Beck et al. (glioma, *in vivo*, n = 12, only applied to 650 nm) [28] were compiled (see aspired literature data in Table 1). Two different types of absorbers were required to tune μ_a simultaneously for both wavelengths because the spectral absorption characteristics of tissue and ink diverge. However, a single scatterer, namely Lipovenös®, was sufficient to model μ_s' at both wavelengths. Phantom ingredient concentrations (Table 2) have been determined from literature data [29] (Lipovenös®) and by absorption spectroscopy (Lambda 40, Perkin Elmer GmbH, Überlingen, Germany) (ink, India ink) and confirmed via integrating sphere measurements (see experimentally achieved data in Table 1).

Table 2 Concentrations of the phantom ingredients.

Phantom ingredient	Concentration [%]
Lipovenös®	1.1 (mass of soybean oil/vol)
ink ("brilliant black 4001")	0.046 (vol/vol)
India ink ("Tusche A")	0.003 (vol/vol)

2.2 Experiments

2.2.1 Phantom experiments

2.2.1.1 Bare-fiber probe

In the empty phantom container, the horizontally mounted capillary was first positioned within the plane spanned by the axes of the two vertically oriented fibers, in the following referred to as *fiber plane*. Then the probe was moved downward until the distal fiber ends were in contact with the capillary surface (uncertainty: ±10 µm) and thus 100 µm away from the capillary lumen. Parts of the experiments were conducted in this coplanar configuration (Figure 2e); alternatively, after defining the vertical probe position, the capillary was turned perpendicular to the fiber plane, then crossing the virtual extension of either the emission fiber (Figure 2f), the detection fiber (Figure 2g), or the probe axis (Figure 2h), i.e. the center line between the two fiber axes representing the main rotation axis of the probe as shown in Figure 2b. The focus of experiments and simulations was on the coplanar configuration, which – due to geometry and functioning of the biopsy needle – bears a higher risk of blood vessel rupture than the perpendicular configurations. After alignment, the phantom liquid was carefully poured into the container and the probe was moved upward by 1800 µm in increments of 100 µm. For each vertical position, a spectrum was recorded. This alignment and measurement procedure was conducted three times for each configuration and inter-fiber distance.

2.2.1.2 Needle probe

In the phantom experiments performed with the needle probe, the capillary was always positioned perpendicular to the probe axis (cf. Figure 8a). The capillary was initially placed about one millimeter above the upper fiber end, at a varying fiber-to-capillary distance between 0.3 mm and 1.9 mm. After adding the phantom liquid, the needle probe was moved upward (in z-direction) by about 5 mm in steps of 0.2 mm. For each z-position, one spectrum was recorded.

2.2.2 Experiments on ex-vivo tissue

Ex-vivo measurements were performed with the needle probe on fresh porcine brain tissue about 1–2 h after slaughtering. The needle was inserted at ten different locations that were obviously not or very poorly perfused ("without blood vessel") and at further ten different locations that were obviously well supplied with blood ("with blood vessel"). For each needle position, one spectrum was recorded.

2.3 Ray tracing simulations

To support and extend the experimental results, Monte Carlo-based ray tracing simulations were performed for the wavelengths 578 nm and 650 nm using TracePro (Version 4.1.7, Lambda Research Corporation, Littleton, MA, USA). The geometric model is illustrated in Figure 3. The used optical parameter sets are listed in Table 3; absorption and scattering coefficients are specified for 578 nm and 650 nm, the refractive index (n) is valid for both wavelengths.

Two different versions of the simulation model were used: either a homogeneous blood-tumor phantom without blood vessel, to which different blood volume fractions (BVF) were applied (Section 2.3.1), or a tumor phantom with blood vessel where diameter, position and orientation (within (coplanar) or perpendicular to the fiber plane) of the blood vessel were varied (Section 2.3.2). For each BVF or fiber-vessel configuration, respectively, three independent simulations with different random number seeds were performed.

2.3.1 Homogeneous blood-tumor phantom

The first version of the simulation model consisted of identical emission and detection fibers, both embedded into a cylindrical phantom that was infinitely large as compared to the local light penetration depth (≤1.7 mm). Depending on the applied BVF, the optical properties of the phantom were calculated as a linear superposition of tumor [26–28] and blood [30] properties, assuming a BVF of 5% to be already included in the optical properties of pure tumor due to its capillary perfusion [31]. Venous and arterial blood with oxygen saturations of 75% and ≥98%, respectively, were examined separately [30]. The fibers, composed of non-absorbing and non-scattering core (n = 1.46) and cladding (n = 1.44) and of a perfectly absorbing and non-scattering coating (n = 1.66), were positioned parallel and symmetrical to the z-axis with an axis-to-axis spacing of 2 mm. A circular light source (diameter: 0.2 mm), which was positioned in the core of the emission fiber 0.5 mm below the proximal fiber end face (z = 0.5 mm), emitted 10^7 rays. The proximal end face of the detection fiber core (z = 0) served as detector.

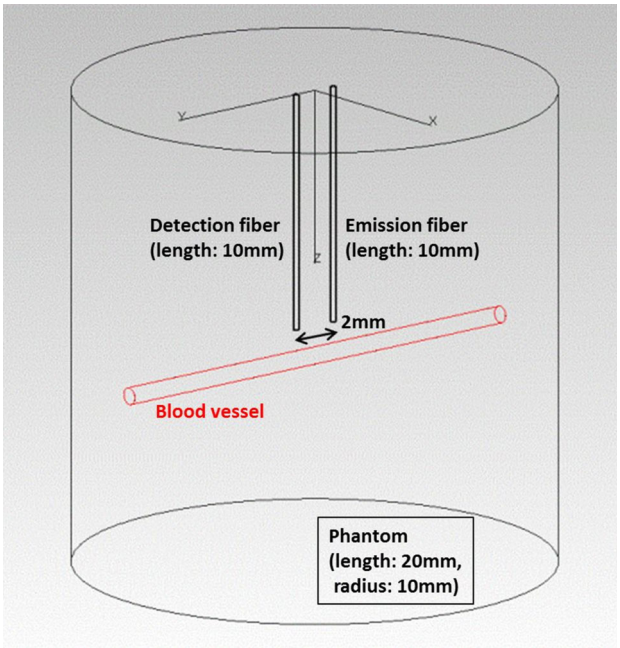

Figure 3 Geometric model used for simulations in a tumor phantom with blood vessel where diameter, position and orientation (within (coplanar) or perpendicular to the fiber plane) of the blood vessel were varied. For simulations in a homogeneous blood-tumor phantom, the blood vessel was removed and different blood volume fractions were attributed to the phantom.

2.3.2 Tumor phantom with blood vessel

In the second version of the simulation model, a blood-vessel mimicking cylinder was additionally in-

Table 3 Refractive index (n), absorption (μ_a) and reduced scattering (μ_s') coefficients of the simulation objects (BVF: blood volume fraction).

Object/Entity		n	μ_a [mm^{-1}]		μ_s' [mm^{-1}]	
		578 nm/650 nm	578 nm	650 nm	578 nm	650 nm
pure tumor (5.0% BVF)		1.4	0.21	0.068	1.8	1.6
blood vessel (100% BVF)	vein	1.3	25.1	0.57	2.1	1.5
	artery	1.3	26.9	0.16	2.3	1.5

serted into the phantom at different orientations and distances from the fibers. The cylinder diameter was varied between 100 µm and 1500 µm. Pure tumor properties (5% BVF [26–28]) were assigned to the phantom, pure blood properties (100% BVF, either venous or arterial [30]) to the vessel-mimicking cylinder. To corroborate the direct comparability with the experimental results, some simulations were performed with a non-absorbing and non-scattering glass wall (thickness: 100 µm, glass type: pure silica, $n = 1.46$) around the vessel-mimicking cylinder. All indicated fiber-to-vessel distances refer to the distance from the blood cylinder inside the glass.

2.4 Data analysis

Data analysis including statistical evaluations was performed with MATLAB (Version R2014b (8.4.0.150421), The MathWorks, Inc., Natick, MA, USA) and SigmaPlot (Version 11.0, Systat Software GmbH, Erkrath, Germany). The experimental raw spectra $I_{raw}(\lambda)$ with intensity values given in counts per ms integration time were corrected by the dark spectra $I_{dark}(\lambda)$ and subsequently divided by the corrected LED emission spectrum $I_{LED}(\lambda) - I_{dark}(\lambda)$ shown in Figure 2d (normalization). Thereafter, the normalized intensity values I_{578}^{norm} (averaged over 6 pixels between 577 nm and 579 nm) and I_{650}^{norm} (averaged between 649 nm and 651 nm) were used to calculate the remission ratio R:

$$R = \frac{I_{578}^{norm}}{I_{650}^{norm}} = \frac{\left\langle \frac{I_{raw}(\lambda) - I_{dark}(\lambda)}{I_{LED}(\lambda) - I_{dark}(\lambda)} \right\rangle_{577-579}}{\left\langle \frac{I_{raw}(\lambda) - I_{dark}(\lambda)}{I_{LED}(\lambda) - I_{dark}(\lambda)} \right\rangle_{649-651}} \quad (1)$$

In case of the simulations, the ratio of the detected fluxes at 578 nm and 650 nm was analogously calculated via Eq. (1), however without dark correction, normalization and averaging. Gaussian error propagation was used to calculate the uncertainty of the remission ratio R. Exponential curve fitting (Levenberg–Marquardt algorithm), statistical significance (unpaired two-tailed t-test, normality (Shapiro–Wilk test) and equal variance of the two groups had been tested beforehand) and correlation (Pearson product-moment correlation) testing were performed via SigmaPlot.

3. Results

3.1 Experiments and simulations with bare fibers

3.1.1 Experiments with blood-filled glass capillary: Dependency on fiber-to-capillary distance, capillary orientation, and inter-fiber distance

The dependency of the experimentally determined remission ratio R on the fiber-to-capillary distance is displayed in Figure 4a for different fiber-probe orientations (bare-fiber probe, inner capillary diameter: 700 µm, inter-fiber distance: 2 mm). In the coplanar configuration, the remission ratio is zero when the fibers are in direct contact with the capillary wall (fiber-to-capillary distance: 100 µm). With increasing fiber-to-capillary distance, the ratio rises up to a saturation level of 0.44. In the perpendicular configurations, the signal depends on the location of the capillary relative to the probe axis: When the capillary crosses the probe axis ("perpendicular, between fibers"), almost identical remission ratios as in the coplanar configuration are obtained for fiber-to-

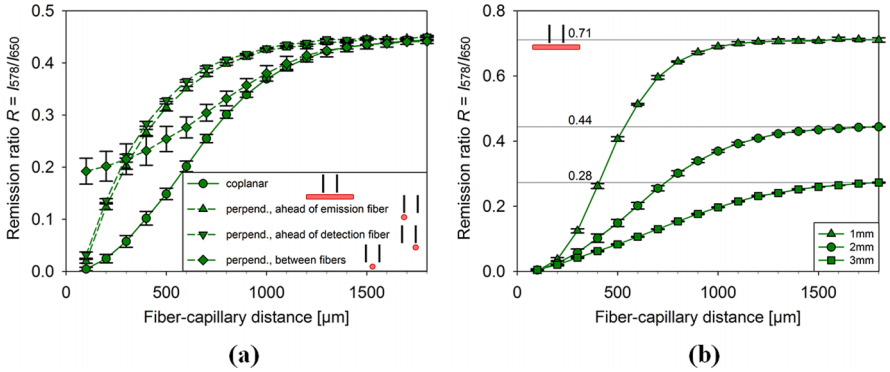

Figure 4 Experimental remission ratio R with the bare-fiber probe and a 700 µm capillary in dependency on the fiber-to-capillary distance for (**a**) different capillary orientations at an inter-fiber distance of 2 mm and (**b**) different inter-fiber distances in the coplanar configuration. Error bars denote standard errors of the means obtained from three measurements after renewed adjustment of the relative probe-capillary orientation.

capillary distances above 1000 µm. Towards smaller distances, the ratio decreases more slowly and reaches a minimum value slightly below 0.2 at the smallest possible fiber-to-capillary distance of 100 µm. When the capillary is positioned directly ahead of the emission or detection fiber, however, the ratio diminishes only slightly for distances down to about 700 µm. Below this distance value, the ratio is subject to a steep decrease and vanishes in the immediate vicinity of the probe.

For the coplanar configuration, the dependency on the fiber-to-capillary distance was additionally investigated by using inter-fiber distances of 1 mm and 3 mm (Figure 4b). In each case, the remission ratio reaches zero for fiber-to-capillary distances of 100 µm. The smaller the inter-fiber distance, the faster the ratio increases with rising fiber-to-capillary distance and the faster the respective saturation level (0.71, 0.44, and 0.28 for 1 mm, 2 mm, and 3 mm inter-fiber distance, respectively) is reached.

3.1.2 Simulations in homogeneous tumor phantom: Dependency on blood volume fraction

The remission ratio R derived from simulations in a homogeneous blood-tumor phantom strongly depends on the BVF (Figure 5a). In a pure tumor phantom (5% BVF), the ratio is 0.48, as determined in six independent simulations. In the following, this result for a tumor without BVF enhancement will be referred to as *background level*. With increasing BVF, the ratio decreases and practically equals zero for BVF values higher than about 10%. In good approximation, the obtained curves can be described by an exponential fit

$$R = a \cdot \exp\left(-b \cdot \mathrm{BVF}[\%]\right) \qquad (2)$$

The resulting fit parameters are $a = 289 \pm 69$ and $b = 1.28 \pm 0.05$ for venous and $a = 437 \pm 89$ and $b = 1.37 \pm 0.04$ for arterial blood, respectively. In Figure 5b, a double-logarithmic plot of the same data reveals that venous blood leads to higher R values than arterial blood; this difference increases with rising BVF.

3.1.3 Simulations in tumor phantom with blood vessel: Dependency on fiber-to-vessel distance, vessel diameter and oxygen saturation

In Figure 6, the results of the simulations in the tumor phantom with blood vessel (coplanar configuration, without surrounding glass wall, inter-fiber distance: 2 mm) are shown. While the simulated remission ratios R for arteries with a diameter of 700 µm (Figure 6a) match the experimental results in the coplanar configuration (comparison shown in Figure 7a), the simulated remission ratios for veins are systematically higher. The indicated background level of 0.48 was taken from Section 3.1.2. As shown in Figure 6b for three exemplary fiber-to-vessel distances, the remission ratio is considerably higher for a blood vessel diameter of 100 µm than for larger diameters (500–1500 µm) where it remains approximately constant. Again, veins lead to a higher remission ratio than arteries.

3.1.4 Consistency of experimental and simulation results

Excellent accordance of the results obtained in experiments and simulations with arteries was obtained

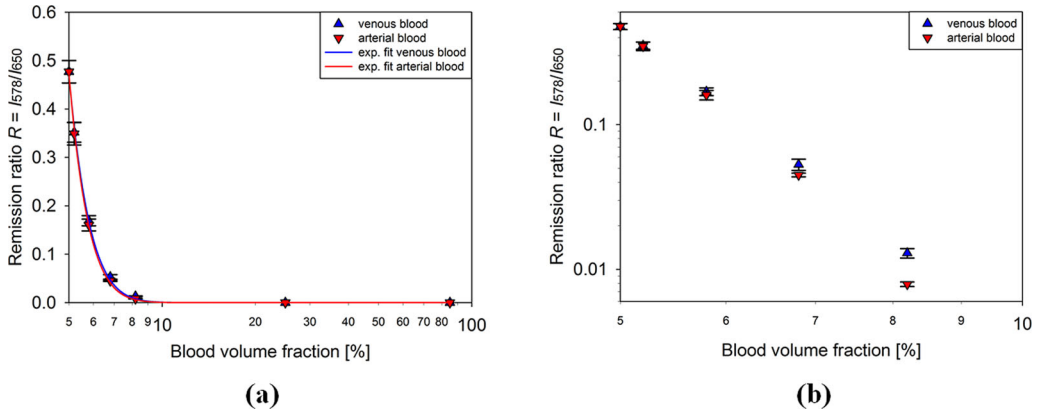

Figure 5 Simulated remission ratio R for the bare-fiber probe (2 mm inter-fiber distance) in dependency on the BVF in the homogeneous blood-tumor phantom. (**a**) Semi-logarithmic plot. (**b**) Double-logarithmic plot. Error bars denote standard errors of the means obtained from three simulations with different random number seeds.

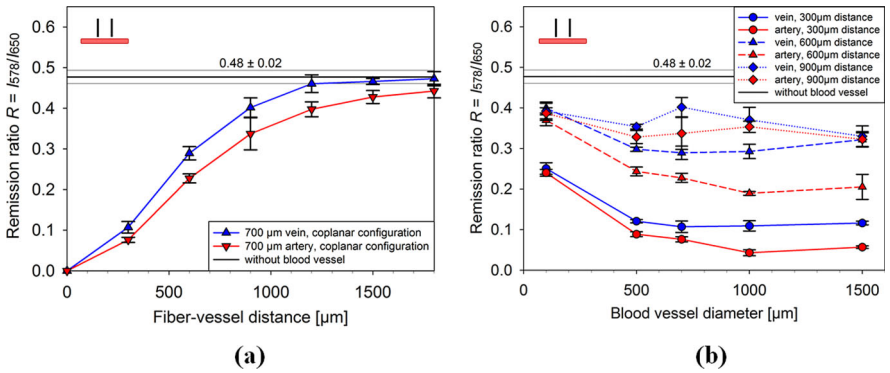

(a) **(b)**

Figure 6 Simulated remission ratio R for the bare-fiber probe (2 mm inter-fiber distance) in dependency on (**a**) the fiber-to-vessel distance for a blood vessel of 700 µm diameter and (**b**) the blood vessel diameter for three fiber-to-vessel distances. Veins and arteries were considered separately. The blood vessel axis was always positioned within the fiber plane (coplanar configuration) and the vessel was not surrounded by a glass wall. Error bars denote standard errors of the means obtained from three simulations with different random number seeds.

for all orientations of the capillary or vessel, respectively, with regard to the bare-fiber probe (Figure 7); no systematic difference was found between the two versions of the simulation model (with/without glass). The correlation coefficients (Pearson's r) of all possible method pairs (experiment vs. simulation with glass, experiment vs. simulation without glass, simulation with glass vs. simulation without glass) for the respective orientations varied between 0.981 and 0.999.

3.2 Experiments with the needle probe

3.2.1 Experiments on tumor phantom with blood-filled glass capillary: Dependency on fiber-to-capillary distance and z-position of the needle probe

In Figure 8b, remission ratio profiles obtained by moving the needle probe along the z-direction are

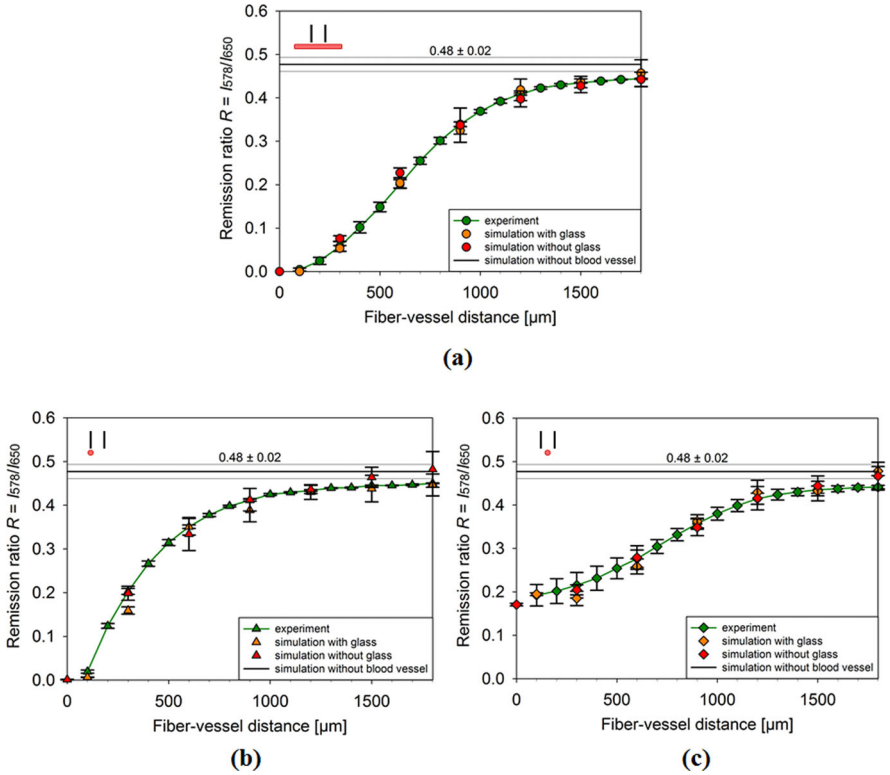

(a)

(b) **(c)**

Figure 7 Comparison of experiment and simulation (with and without glass wall around the blood cylinder, in each case filled with arterial blood) based on results for the remission ratio R obtained with the bare-fiber probe (inter-fiber distance: 2 mm) and a capillary/blood vessel of 700 µm diameter (**a**) within the fiber plane (coplanar), (**b**) perpendicular to the fiber plane ahead of the emission fiber and (**c**) perpendicular to the fiber plane between the fibers.

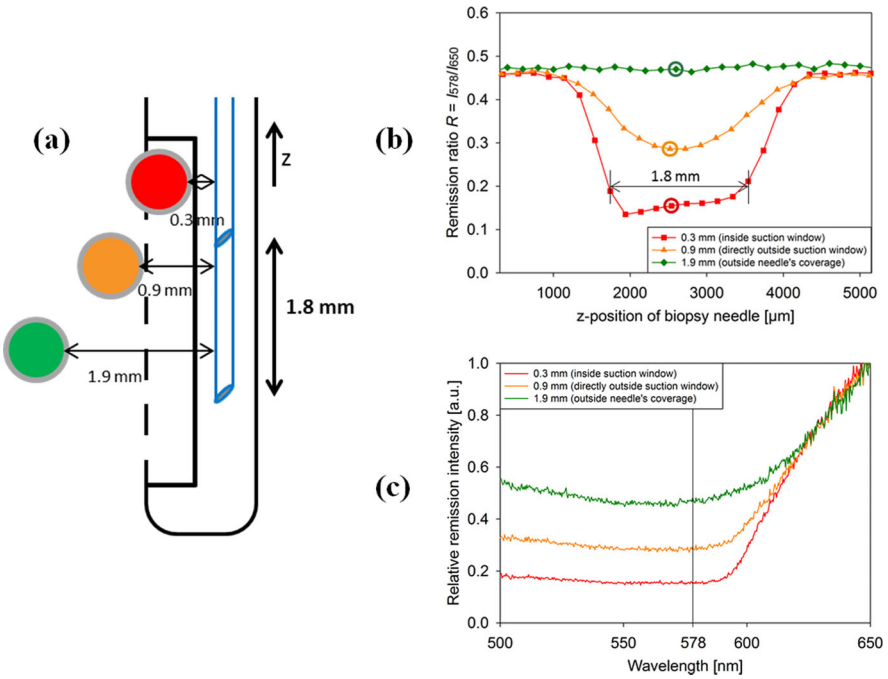

Figure 8 (**a**) Illustration of the experiments with the needle probe on the tumor phantom for three different fiber-to-capillary distances. After adjusting the fiber-to-capillary distance, the needle was moved in *z*-direction. The capillary orientation was perpendicular to the drawing plane. (**b**) Experimental results. The three fiber-to-capillary distances are indicated by the colors red, orange and green (cf. Figure 8a). (**c**) Three representative normalized remission spectra (intensity at 650 nm was set to 1), representing the three fiber-to-capillary distances indicated by the colors red, orange and green (cf. Figure 8a). The corresponding *z*-positions of the biopsy needle are marked in Figure 8b. The ordinate values at 578 nm (indicated by the vertical line) are equal to the remission ratios *R*.

shown for three fiber-to-capillary distances (Figure 8a) representing the model cases "vessel inside suction window (high risk)" (red), "vessel directly outside suction window (borderline case)" (orange) and "vessel outside needle's coverage (no risk)" (green). Representative normalized remission spectra (one for each of these cases) are shown in Figure 8c. In the first case, the following blood-vessel indicating signature is clearly visible: The remission ratio *R* abruptly decreases from the background level 0.48 (representing homogeneous pure brain tumor tissue) to about 0.15 when passing the capillary with the end of the emission fiber (upper fiber in Figure 8a) at $z \approx 1800$ µm. Afterwards, the ratio stays almost constant as long as the capillary is located between the two fiber ends (plateau), i.e. up to $z \approx 3600$ µm, and then re-increases to the background level after passing the capillary with the end of the detection fiber. The occurrence of the plateau with a length slightly below 1.8 mm (distance between fiber ends) is due to the selected fiber-to-capillary distance of 0.3 mm – a value that is close to the intersection point of the three curves in Figure 4a that represent the perpendicular configurations. For direct fiber-capillary contact, one would have expected two minima with a spacing of

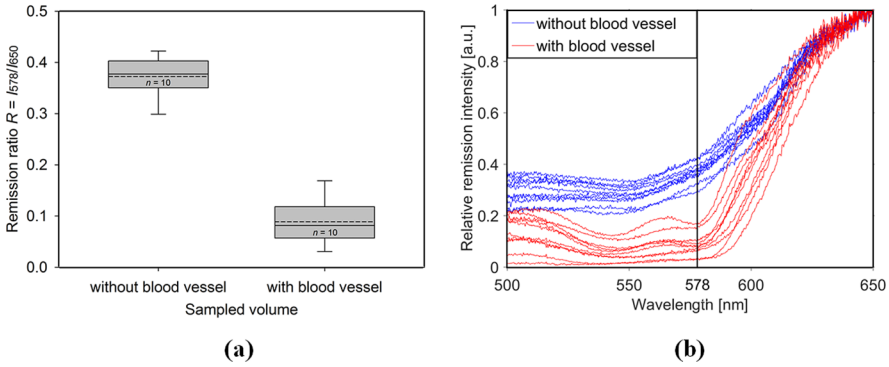

Figure 9 (**a**) Remission ratio *R* acquired with the needle probe on *ex-vivo* porcine brain tissue. The box plots display the median (solid line) and the average (dashed line) as well as the 5th, the 25th, the 75th and the 95th percentiles of the *R* values obtained at ten different locations within the tissue. The signal difference between biopsy volumes with and without blood vessel is statistically significant ($p \leq 0.001$). (**b**) Normalized remission spectra (intensity at 650 nm was set to 1), whose ordinate values at 578 nm (indicated by the vertical line) are equal to the remission ratios *R*.

1.8 mm. In the second case, the ratio only decreases from 0.48 to 0.3 with a minimum between the two fiber ends. Still, a blood vessel would be detectable in this borderline case. In the third case, the ratio does not deviate from the background level at any z-position, i.e. a blood vessel at this distance, which could not be sheared off during biopsy sampling, would not show up in the optical signal and thus not impair the biopsy procedure. All these findings are in reasonable accordance with the bare-fiber results (Figure 4a).

3.2.2 Experiments on ex-vivo porcine brain tissue: Dependency on needle position with respect to tissue vasculature

In porcine brain tissue, regions with and without blood vessel could well be distinguished with the needle probe (Figure 9a). The remission ratio R was significantly ($p \leq 0.001$) lower when the probed tissue volume contained one (or more) blood vessel(s) (average values: 0.09 vs. 0.37). The normalized remission spectra (Figure 9b) could also be clearly discriminated with regard to the presence of blood vessels; in most spectra obtained on tissue volumes with blood vessel, the characteristic absorption maxima of oxygenated hemoglobin at around 540 nm and 580 nm were visible. The remission ratio in tissue regions without blood vessel was subject to a moderate absolute standard deviation ($n = 10$) of 0.04 (relative standard deviation with respect to the average: 11%) and its average value 0.37 deviated by about 20% from the background level obtained in phantom experiments and simulations, which ranged from 0.44 to 0.48. This accuracy is compatible with the general accuracy limits of tissue optical properties. The absolute standard deviation of the remission ratio in tissue regions with blood vessel(s) was 0.05 ($n = 10$), the relative standard deviation was 52%.

4. Discussion

4.1 Validity of experiments and simulations

A priori, the experimental setting is best represented by the simulations with glass wall around the blood cylinder. Real blood vessels, however, are in principle better represented by the simulations without glass wall, provided that distances are measured from the inner surfaces of the vessel walls as it was the case in all presented experiments and simulations. This is due to the optical properties of vascular walls, which differ significantly from those of glass, but only moderately (20–60%) from those of brain tissue [32] (aorta values taken as reference for vascular walls, determined *in vitro*, $n = 9$). But as a consequence of the displayed accordance of the results from all three methods (Figure 7), experiments and simulations with glass can be regarded as representing real blood vessels in tumor tissue equally well as the simulations without glass.

4.2 Dependency of the remission ratio on the investigated parameters

4.2.1 Impact of fiber-to-vessel distance for different blood vessel orientations

The dependencies of the remission ratio R on blood vessel orientation and fiber-to-vessel distance (Figure 4a) can be explained by the spatial distribution of paths associated with photons that emanate from the emission fiber and arrive at the detection fiber as sketched in Figure 10. This distribution, which is well-known in diffuse reflectance spectroscopy as *photon banana*, can be derived from Monte Carlo simulations [33, 34]. The flux line density, encoding the density of the above-mentioned photon paths in case no blood vessel is present, is a measure for the sensitivity of the recorded remission spectra, and thus the remission ratio R, to the local absorption. To determine the impact of a blood vessel on the detected remission ratio R, the local absorption, weighted with the local line density, has to be integrated over the entire vessel volume. In other words: the higher the line density in a certain region, the stronger the reduction of the detected remission ratio if a blood vessel with given diameter is located in that region.

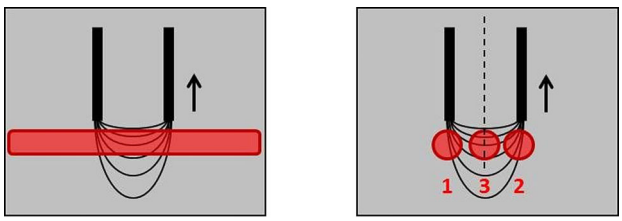

Figure 10 Flux line plot representing the stochastic spatial distribution of paths associated with photons that were emitted from one and detected with the other fiber (*photon banana*). The line density encodes the density of photon paths. Superimposed is a blood vessel (red) (**a**) within (coplanar) or (**b**) perpendicular to the fiber plane (positioned either directly ahead of the emission (1) or detection (2) fiber or between the two fibers (3); dashed line: probe axis). The arrow indicates the direction in which the fiber-probe is moved to adjust the fiber-to-vessel distance.

From Figure 10a, it can be discerned for the coplanar configuration that with increasing distance from the fiber tips, the line density decreases, so the presence of a blood vessel has a weaker influence on the recorded remission signal, which leads to an increase of the remission ratio (cf. Figure 4a). In the perpendicular configurations (Figure 10b), the symmetry with respect to the probe axis leads to an identical influence on the remission signal, whether the blood vessel is placed ahead of the emission (position 1) or detection (position 2) fiber: Starting at almost zero when the probe is in contact with the blood vessel, the remission ratio R undergoes a steep increase with rising fiber-to-vessel distance, followed by a convergence to the background level (cf. Figure 4a). When placed between the fibers (position 3), however, the blood vessel has a lower impact in the vicinity of the probe (lower line density than for positions 1 or 2), leading to a remission ratio of about 0.2, which is followed by a relatively shallow increase with rising fiber-to-vessel distance as compared to positions 1 or 2 (weaker decrease of line density than for positions 1 or 2). As a consequence, the coplanar orientation of a blood vessel leads to the best traceability. Up to a fiber-to-vessel distance of about 300 µm, a perpendicularly orientated blood vessel is better detectable directly ahead of either the emission or the detection fiber than between the fibers; for fiber-to-vessel distances larger than 300 µm, this relation is inverted.

4.2.2 *Impact of blood vessel diameter*

With increasing blood vessel diameter (and constant fiber-to-vessel distance), a larger volume in front of the fibers is covered with blood (Figure 10a). Consequently, thicker vessels are better detectable. This effect considerably decreases for blood vessel diameters larger than 500 µm (cf. Figure 6b) when regions with lower line densities are additionally covered by the vessel. Up to a fiber-to-vessel distance of 900 µm (dotted curve, Figure 6b), which approximately corresponds to the depth of the needle window (cf. Figure 2c), blood vessels in the coplanar configuration with a diameter down to at least 500 µm, possibly also 100 µm, should be discernible.

4.2.3 *Impact of inter-fiber distance*

With increasing inter-fiber distance, the background level of the remission ratio R recorded at large fiber-to-capillary distances decreases (Figure 4b). This is due to the absorption in the phantom, which is much higher at 578 nm than at 650 nm (cf. Table 1) so that the shorter wavelength is more strongly suppressed with rising inter-fiber distance. The phenomenon that for a larger inter-fiber distance, the respective background level of R is reached at larger fiber-to-capillary distances (cf. Figure 4b) can also be explained with Figure 10a as an increasing inter-fiber distance leads to a lower line density gradient in the vicinity of the probe axis. As a consequence, probes with larger inter-fiber distances exhibit a higher sensitivity to distant blood vessels, albeit at the cost of lower intensities since more absorption events occur between the two fibers. With regard to the development and optimization of a biopsy-needle device, the suction window should not be considerably longer than the selected inter-fiber distance because the vessel detectability to the respective outer sides of both fiber tips rapidly decreases as shown in Figure 8b where the inter-fiber distance was 1.8 mm.

4.2.4 *Impact of oxygen saturation*

The simulations with blood vessel demonstrate that an artery in the vicinity of the probe reduces the remission ratio R more strongly than a vein (Figure 6). Thereby, the relative deviation of the arterial R from the venous R increases with decreasing fiber-to-vessel distance, i.e. with rising impact of the blood vessel on the detected remission spectra, from 6.4% at a distance of 1800 µm to 29% at a distance of 300 µm. This result is not surprising as arterial blood exhibits a higher absorption coefficient at 578 nm and a lower absorption coefficient at 650 nm than venous blood (cf. Table 3). Due to the definition of the remission ratio R according to Eq. (1), both effects add up to a reduced R for arteries as compared to veins, especially when the blood vessel is close to the fiber probe. Thus, using this method, arteries can be detected more easily than veins as they induce a remission ratio R that deviates more strongly from the background level of about 0.48. This might even improve the safety of the technique as artery ruptures are presumably more critical than vein ruptures.

In the homogeneous blood-tumor phantom, arterial blood leads to a lower remission ratio R than venous blood, too (Figure 5). In the semi-logarithmic plot of Figure 5a, the different blood types can hardly be discriminated because the remission ratios already converge to zero for relatively small BVF values around 10%. However, an increasing relative deviation of R with rising BVF can be discerned in the corresponding double-logarithmic plot (Figure 5b).

4.3 Reliability and limitations of the technique

4.3.1 Variations of tissue optical properties and decision threshold

By means of the presented technique, a blood vessel is recognized by the reduction of the remission ratio R from the far-distance background level that it induces. This suggests determining a ratio threshold above which biopsy sampling is deemed to be allowed and below which the surgeon would be well advised to better take the biopsy at a different site because a blood vessel could otherwise be injured. For safety purposes, this threshold should be chosen as high as possible. On the other hand, it should be sufficiently well below the background level to maintain the practicability of the technique. Furthermore, the threshold has to be specifically calibrated for each device as the background level depends on the exact inter-fiber distance (Figure 4b).

The definition of a reasonable threshold for a given probe requires assessing intra- and inter-individual variations of tissue optical properties (comprising the three tissue types tumor and – depending on the measurement position – also white and gray matter) as shown by the following rough estimation of the detected background level (and its uncertainty), which refers to the situation where no blood vessel is close enough to influence the remission ratio R:

For a time-independent point source, the solution of the diffusion equation for the photon flux is proportional to

$$\frac{1}{D(\lambda)\cdot r}\cdot \exp\left[-\mu_{\mathrm{eff}}(\lambda)\cdot r\right] \tag{3}$$

where r is the source-detector distance and $D(\lambda)=1/(3\cdot(\mu_a(\lambda)+\mu_s'(\lambda)))$ and $\mu_{\mathrm{eff}}(\lambda)=\sqrt{\mu_a(\lambda)/D(\lambda)}$ represent diffusion and effective attenuation coefficients at a given wavelength λ, respectively [35]. Substitution into Eq. (1) leads to a remission ratio of

$$R=\frac{D(650\ \mathrm{nm})}{D(578\ \mathrm{nm})}\cdot\exp(-\Delta\mu_{\mathrm{eff}}\, r) \tag{4}$$

with $\Delta\mu_{\mathrm{eff}}=\mu_{\mathrm{eff}}(578\ \mathrm{nm})-\mu_{\mathrm{eff}}(650\ \mathrm{nm})$. Since $\mu_s'\gg\mu_a$ (as assumed in the diffusion approximation), the ratio of the diffusion coefficients can be approximated by the reciprocal ratio of the respective reduced scattering coefficients, which is almost constant for all three tissue types, taking values between 1.1 and 1.2 [26, 27]. This can be explained by the constant spectral scattering characteristics of cell and organelle membranes, which are presumed to be responsible for light scattering in tissue [36]. Consequently, the remission ratio R mainly depends on the difference $\Delta\mu_{\mathrm{eff}}$:

$$R\propto\exp\left(-\Delta\mu_{\mathrm{eff}}\, r\right) \tag{5}$$

Based on the data reported for all three tissue types (tumor, white and gray matter) [26, 27], the standard deviation of $\Delta\mu_{\mathrm{eff}}$ amounts to about 50% of its mean value. Assuming a background level of 0.48 for R as determined for an inter-fiber distance of 2 mm via simulation (Figure 6), a $\Delta\mu_{\mathrm{eff}}$ variation of 50% would yield remission ratios of $0.48^{(1-0.5)}=0.69$ and $0.48^{(1+0.5)}=0.33$, respectively. Hence, a threshold around 0.3, which corresponds to a fiber-to-vessel distance of about 800 µm in the coplanar configuration (cf. Figure 4a) and thus to the depth of the needle window (cf. Figure 2c), seems to be a reasonable choice for a probe with 2 mm inter-fiber distance.

4.3.2 Discrimination between blood vessel and blood in the interstitium

The differentiation between blood vessels and blood in the interstitium leaking from an injured minor blood vessel in the vicinity of the biopsy site remains an issue of the technique in the presented form. This could be problematic as even a small increase of the BVF has a significant effect on the remission ratio (Figure 5). Blood withdrawing by suction before tissue excision or a time-dependent signal acquisition might be possible solutions. The first measure could be implemented with a suction tube integrated into the biopsy needle; in the second case, one could identify blood vessels by means of time-dependent oscillations in the remission ratio due to the pulsed blood flow and the thereby induced change in vessel diameter. The principle of this photoplethysmographic measurement is already widely used in pulse oximeters [37–39] and is potentially also applicable to cerebral veins [37, 40, 41].

4.4 Clinical applicability

The presented remission spectrometric technique was conceived as a simple and readily realizable alternative to existing concepts regarding blood vessel detection. It appears to have a high clinical potential similar to LDF, which has already been tested clinically for tissue discrimination and blood perfusion mapping during deep brain stimulation. Based on the presented results, it provides a sensitivity comparable to Doppler sonography (minimum blood

vessel diameter: 100 µm/maximum distance: 1 mm) [18], ICG (600 µm/1 mm) [20] or iOT (300 µm/1–2 mm) [22].

In addition, the proposed technique offers several practical advantages: Firstly, due to its integration into the biopsy needle, the fiber probe does not have to be removed from the biopsy channel for tissue sampling, which benefits the clinical workflow and assures a maximal congruence of optically and mechanically sampled volumes. In opposition to LDF, no laser with high coherence length [42, 43], but only a less expensive LED is required. Furthermore, data acquisition is possible within 1s, in opposition to LDF and iOT where several seconds [19] and several minutes [22] are required, respectively. Furthermore, compared to iOT, a much simpler probe design is possible as only two instead of 24 fibers are needed [21, 22]. Finally, in contrast to the ICG technique, no drug injection is necessary, which would bear further risks and most importantly would limit the time period during which blood vessel detection is possible to only a few minutes as the retention time of ICG in the blood circulation is limited [44].

The experimental details of the measurement technique can of course still be modified if desired. For instance, evaluation wavelengths other than 578 nm and 650 nm are conceivable: Using the isosbestic points in the hemoglobin absorption spectra where the extinction coefficients of oxygenated and deoxygenated hemoglobin are identical, i.e. approximately 580 nm and 800 nm (cf. Figure 1b), would make the remission ratio independent of the oxygen saturation of the blood vessel. Thereby, arteries and veins could be detected with identical sensitivity and statistical analyses of in-vivo data regarding parameters like e.g. the vessel diameter could be simplified. In any case, medical approval is still required before the proposed technique can be brought to clinical practice.

5. Conclusion

We suggest dual-wavelength remission spectrometry by means of a two-fiber probe to detect blood vessels during stereotactic biopsy and thus minimize the risk of hemorrhages. Based on the presented results, blood vessels of ≥100–500 µm diameter should be well discernible, independently of their orientation, up to a distance of about 800 µm, i.e. within the suction window of a conventional biopsy needle where the risk of a rupture is present. For this sensing direction, side-view fibers are needed. Beyond that, blood vessels ahead of the biopsy needle might be detected with an additional bare-fiber probe integrated into the needle. Blood vessels more than 1500 µm away from the probe do not reduce the remission ratio and will thus not lead to false-positive results.

This simple and easily implementable method shows the potential to significantly increase the safety of stereotactic biopsy. Beyond this scope of application, the measurement principle could also be used for other surgical procedures. First experiments on *ex-vivo* tissue have confirmed its functionality, but further research (ideally *in vivo*) is still required to optimize the technique.

Acknowledgements Funding support by the German Ministry of Education and Research (BMBF) and the Russian Foundation for Assistance to Small Innovative Enterprises (FASIE) under grant numbers 01DJ14012A and 01DJ14012B (GLIOTAX) is gratefully acknowledged. The authors want to thank Werner Preisser, Armin Hadzimujic and Thomas Pongratz for valuable technical support.

Author biographies Please see Supporting Information online.

References

[1] H. Malone, J. Yang, D. L. Hershman, J. D. Wright, J. N. Bruce, and A. I. Neugut, World neurosurgery **84**(4), 1084–1089 (2015).
[2] M. L. Goodenberger and R. B. Jenkins, Cancer Genet **205**(12), 613–621 (2012).
[3] Q. T. Ostrom, L. Bauchet, F. G. Davis, I. Deltour, J. L. Fisher, C. E. Langer, M. Pekmezci, J. A. Schwartzbaum, M. C. Turner, K. M. Walsh, M. R. Wrensch, and J. S. Barnholtz-Sloan, Neuro Oncol **16**(7), 896–913 (2014).
[4] H. Ohgaki, Methods Mol Biol **472**, 323–342 (2009).
[5] M. Weller, R. Stupp, G. Reifenberger, A. A. Brandes, M. J. van den Bent, W. Wick, and M. E. Hegi, Nat Rev Neurol **6**(1), 39–51 (2010).
[6] S. Eigenbrod, R. Trabold, D. Brucker, C. Erös, R. Egensperger, C. La Fougere, W. Göbel, A. Rühm, H. A. Kretzschmar, J. C. Tonn, J. Herms, A. Giese, and F. W. Kreth, Acta Neurochir (Wien) **156**(8), 1427–1440 (2014).
[7] C. W. Brennan, R. G. Verhaak, A. McKenna, B. Campos, H. Noushmehr, S. R. Salama, S. Zheng, D. Chakravarty, J. Z. Sanborn, S. H. Berman, R. Beroukhim, B. Bernard, C. J. Wu, G. Genovese, I. Shmulevich, J. Barnholtz-Sloan, L. Zou, R. Vegesna, S. A. Shukla, G. Ciriello, W. K. Yung, W. Zhang, C. Sougnez, T. Mikkelsen, K. Aldape, D. D. Bigner, E. G. Van Meir, M. Prados, A. Sloan, K. L. Black, J. Eschbacher, G. Finocchiaro, W. Friedman, D. W. Andrews, A. Guha, M. Iacocca, B. P. O'Neill, G. Foltz, J. Myers, D. J. Weisenberger, R. Penny, R. Kucherlapati, C. M. Perou, D. N. Hayes, R. Gibbs, M. Marra, G. B. Mills, E. Lander, P. Spellman, R. Wilson, C. Sander, J. Weinstein, M. Meyerson, S. Gabriel, P. W. Laird, D. Haussler, G. Getz, and L. Chin, Cell **155**(2), 462–477 (2013).

[8] J. S. Smith, A. Perry, T. J. Borell, H. K. Lee, J. O'Fallon, S. M. Hosek, D. Kimmel, A. Yates, P. C. Burger, B. W. Scheithauer, and R. B. Jenkins, J Clin Oncol **18** (3), 636–645 (2000).
[9] N. A. Markwardt, N. Haj-Hosseini, B. Hollnburger, H. Stepp, P. Zelenkov, and A. Rühm, J Biophotonics, doi: 10.1002/jbio.201500195 (2015).
[10] S. A. Prahl, Optical Absorption of Hemoglobin, tabulated data compiled from various sources (1999), http://omlc.ogi.edu/spectra/hemoglobin.
[11] A. V. Kulkarni, A. Guha, A. Lozano, and M. Bernstein, J Neurosurg **89**(1), 31–35 (1998).
[12] M. J. McGirt, G. F. Woodworth, A. L. Coon, J. M. Frazier, E. Amundson, I. Garonzik, A. Olivi, and J. D. Weingart, J Neurosurg **102**(5), 897–901 (2005).
[13] R. Dammers, I. K. Haitsma, J. W. Schouten, J. M. Kros, C. J. Avezaat, and A. J. Vincent, Acta Neurochir (Wien) **150**(1), 23–29 (2008).
[14] M. Nishihara, T. Sasayama, H. Kudo, and E. Kohmura, The Kobe journal of medical sciences **56**(4), E148–E153 (2011).
[15] A. A. Shakal and E. A. Mokbel, J Neurol Surg A Cent Eur Neurosurg **75**(3), 177–182 (2014).
[16] D. Kondziolka, A. D. Firlik, and L. D. Lunsford, Neurol Clin **16**(1), 35–54 (1998).
[17] R. Grossman, S. Sadetzki, R. Spiegelmann, and Z. Ram, Acta Neurochir (Wien) **147**(6), 627–631 (2005).
[18] J. Gilsbach, M. Mohadjer, and F. Mundinger, Acta Neurochir (Wien) **89**(1–2), 77–79 (1987).
[19] K. Wardell, S. Hemm-Ode, P. Rejmstad, and P. Zsigmond, Stereotact Funct Neurosurg **94**(1), 1–9 (2016).
[20] W. Göbel, D. Brucker, Y. Kienast, A. Johansson, G. Kniebühler, A. Rühm, S. Eigenbrod, S. Fischer, M. Goetz, F. W. Kreth, A. Ehrhardt, H. Stepp, K. M. Irion, and J. Herms, Opt Express **20**(24), 26117–26126 (2012).
[21] A. Goyette, J. Pichette, M. A. Tremblay, A. Laurence, M. Jermyn, K. Mok, K. D. Paulsen, D. W. Roberts, K. Petrecca, B. C. Wilson, and F. Leblond, Opt Lett **40**(2), 170–173 (2015).
[22] J. Pichette, A. Goyette, F. Picot, M. A. Tremblay, G. Soulez, B. C. Wilson, and F. Leblond, Biomed Opt Express **6**(11), 4238–4254 (2015).
[23] K. Wardell, P. Blomstedt, J. Richter, J. Antonsson, O. Eriksson, P. Zsigmond, A. T. Bergenheim, and M. I. Hariz, Stereotact Funct Neurosurg **85**(6), 279–286 (2007).
[24] K. Wardell, P. Zsigmond, J. Richter, and S. Hemm, Neurosurgery **72**(2 Suppl Operative), 127–140; discussion 140 (2013).
[25] Directive 2006/25/EC of the European Parliament and of the Council of 5 April 2006 on the minimum health and safety requirements regarding the exposure of workers to risks arising from physical agents (artificial optical radiation) (19th individual Directive within the meaning of Article 16(1) of Directive 89/391/EEC) <http://eur-lex.europa.eu/legal-content/EN/TXT/PDF/?uri=CELEX:02006L0025-20140101&from=EN>
[26] S. C. Gebhart, W. C. Lin, and A. Mahadevan-Jansen, Phys Med Biol **51**(8), 2011–2027 (2006).
[27] A. N. Yaroslavsky, P. C. Schulze, I. V. Yaroslavsky, R. Schober, F. Ulrich, and H. J. Schwarzmaier, Phys Med Biol **47**(12), 2059–2073 (2002).
[28] T. J. Beck, W. Beyer, T. Pongratz, W. Stummer, R. Waidelich, H. Stepp, S. Wagner, and R. Baumgartner, in: Proc. SPIE, Photon Migration and Diffuse-Light Imaging, 2003.
[29] R. Michels, F. Foschum, and A. Kienle, Opt Express **16**(8), 5907–5925 (2008).
[30] N. Bosschaart, G. J. Edelman, M. C. Aalders, T. G. van Leeuwen, and D. J. Faber, Lasers Med Sci **29**(2), 453–479 (2014).
[31] A. Rühm, W. Göbel, R. Sroka, and H. Stepp, Photodiagnosis Photodyn Ther **11**(3), 307–318 (2014).
[32] V. Tuchin, Tissue Optics – Light Scattering Methods and Instruments for Medical Diagnosis (SPIE, Bellingham, Washington, USA, 2015), pp. 247–294.
[33] I. J. Bigio and S. Fantini, Quantitative Biomedical Optics (Cambridge University Press, Cambridge, UK, 2016), pp. 229ff., esp. Fig. 8.2.
[34] C. Mansouri and N. H. Kashou, Conf Proc IEEE Eng Med Biol Soc **2009**, 1457–1460 (2009).
[35] L. Wang and H.-I. Wu, Biomedical Optics: Principles and Imaging (John Wiley & Sons, Inc., Hoboken, NJ, USA, 2007), pp. 98–99.
[36] B. W. Pogue and M. S. Patterson, J Biomed Opt **11**(4), 041102 (2006).
[37] M. Nitzan, A. Romem, and R. Koppel, Medical devices **7**, 231–239 (2014).
[38] K. H. Shelley, Anesthesia and analgesia **105**(6 Suppl), S31–S36 (2007).
[39] J. Allen, Physiological measurement **28**(3), R1–R39 (2007).
[40] A. S. Echiadis, V. P. Crabtree, J. Bence, L. Hadjinikolaou, C. Alexiou, T. J. Spyt, and S. Hu, Physiological measurement **28**(8), 897–911 (2007).
[41] K. H. Shelley, D. Tamai, D. Jablonka, M. Gesquiere, R. G. Stout, and D. G. Silverman, Anesthesia and analgesia **100**(3), 743–747 (2005).
[42] G. E. Nilsson, E. G. Salerud, N. O. T. Strömberg, and K. Wardell, Laser Doppler perfusion monitoring and imaging. Biomedical Photonics Handbook (editor: Tuan Vo-Dinh): Chapter 15 (CRC Press Boca Raton, Florida, USA, 2003), pp. 15.1–15.24
[43] I. Fredriksson, C. Fors, and J. Johansson, Laser Doppler Flowmetry – a Theoretical Framework, Department of Biomedical Engineering, Linköping University (2007), www.imt.liu.se/bit/ldf/ldfmain.html.
[44] A. Hagen, D. Grosenick, R. Macdonald, H. Rinneberg, S. Burock, P. Warnick, A. Poellinger, and P. M. Schlag, Opt Express **17**(19), 17016–17033 (2009).